Optical Materials 148 (2024) 114851

Contents lists available at ScienceDirect

Optical Materials

journal homepage: www.elsevier.com/locate/optmat

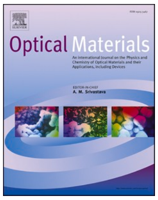

Research Article

Cd-supported CuO-ZnO binary oxide thin films: Synthesis, microstructural, and optoelectronic properties

Halimenur Satılmış [a], Merve Acar [a], Raşit Aydın [a,*], Abdullah Akkaya [b], Osman Kahveci [c], Bünyamin Şahin [d,e], Enise Ayyıldız [c]

[a] Department of Physics, Faculty of Sciences, Selçuk University, Konya, Turkey
[b] Mucur Technical Vocational Schools, Tech. Prog. Department, Kırşehir Ahi Evran University, Kırşehir, Turkey
[c] Department of Physics, Faculty of Sciences, Erciyes University, Kayseri, Turkey
[d] Department of Basic Sciences, Faculty of Engineering, Necmettin Erbakan University, Konya, Turkey
[e] BITAM-Science and Technology Research and Application Center, Necmettin Erbakan University, Konya, Turkey

ARTICLE INFO

Keywords:
Binary oxides
ZnO film
CuO film
Cd-doping
Bandgap
Resistivity

ABSTRACT

This article reports the synthesis of low-cost, repeatable, and low-processing-temperature Cd-doped copper oxide (CuO)/zinc oxide (ZnO) binary nanocomposite thin films. Binary CuO– ZnO thin film samples were fabricated using the solution-based SILAR method. We primarily report the examination of a Cd-doping-induced improvement in the optical and electrical performances of CuO–ZnO binary samples at room temperature by tailoring the surface morphology and crystalline structure. The experimental results confirmed the formation of pure nanostructured composites. The estimated Eg is approximately 2.26 eV, which increases with increasing Cd content in the growth bath. The transmittance spectra exhibit an increase in the transmittance from 58 % to 72 % as the Cd content increases, while the contact resistivity varies from ~2.97 to ~22.17 MΩ□. The wider optical bandgap energy is exclusively significant for allowing the designed materials to operate at much higher temperature conditions. The obtained outcome could be used to enhance the impression of photovoltaic devices.

1. Introduction

Nanostructured metal oxide (MO) thin films have attracted considerable attention in the last decade because of their non-toxicity, high stability, high surface area, abundant availability, low fabrication costs, and favorable electrical, optical, magnetic, and catalytic properties [1–4]. These unique properties make them excellent candidates for various technological applications, such as gas sensors, solar cells, lithium batteries, and photocatalysts [5–8]. Among these MOs, zinc oxide (ZnO) is an n-type semiconductor with a wurtzite crystal lattice structure with high exciton binding energy (~60 meV) and wide band gap value (~3.3 eV) [9,10]. Copper oxide (CuO), another MO, is a p-type semiconductor with a monoclinic crystal lattice structure, low energy band gap value (~1.22 eV), and excellent chemical stability [11,12].

In recent years, instead of individual MO semiconductor materials, studies on multiple MO semiconductors (nanocomposite (NC) MOs) have attracted the attention of scientists. By mixing two or more MOs, NC MO materials with excellent chemical and physical characteristics and high technological potential can be synthesized. Combining two MOs such as CuO and ZnO can pave the way for new technological applications such as solar cells, sensors, and energy storage by changing the physical properties such as morphology, lattice structure, and size of the resulting binary CuO– ZnO NCs [13–15].

Various methods such as sol–gel, precipitation, pulsed laser deposition, chemical vapor deposition, spray pyrolysis, hydrothermal, magnetron sputtering, and successive ionic layer adsorption and reaction (SILAR) have been used to obtain NC films [16–20]. These techniques were designed to modify the composition, lattice structure, form, and particle size of the NC films produced. Among these procedures, SILAR is a promising method with advantages such as film thickness control, low-temperature deposition, reproducibility, and good adhesion to the substrate. In addition, SILAR is a simple, safe, and cost-effective synthesis method [21–23].

The doping technique is an important approach for modifying the physicochemical properties of NC oxides and is the basis for the emergence of special functionalities for these materials. The incorporation of dopant elements into the lattice of the host CuO and ZnO can significantly affect the crystal structure and surface morphology, which affects

---

[*] Corresponding author.
E-mail address: raydin@selcuk.edu.tr (R. Aydın).

https://doi.org/10.1016/j.optmat.2024.114851
Received 16 November 2023; Received in revised form 3 January 2024; Accepted 4 January 2024

on the physicochemical parameters. Therefore, some research groups have focused on doping composite films with dopants such as Mn, Ag, Yb, N, and Cd to improve their physical properties [24–28]. Among these doping materials, the oxide structure of Cd (polycrystalline nature) is an n-type semiconductor with excellent properties such as high electrical conductivity ≈ 10^3 Ω^{-1} cm^{-1}, strong carrier mobility ~ 142 $cm^2V^{-1}s^{-1}$, low optical band gap ~ 2.5 eV, and wide linear refractive index ~ n = 2.49 [29–31].

To the best of our knowledge, no studies have reported the synthesis of binary CuO–ZnO NC films using a Cd dopant using the SILAR method. Therefore, we used Cd as an additive material in this study. We also studied the effect of Cd at different concentration ratios on physical properties such as the morphological, electrical, and optical properties of CuO– ZnO binary NC films. The details are discussed in the following sections.

2. Experimental details

In this study, un-doped and Cd-doped binary CuO– ZnO NC films were obtained on glass substrates using the SILAR procedure. Copper (II) chloride dehydrate ($Cl_2CuH_4O_2$; ≥99.0 %; CAS Number: 10125-13-0) and zinc acetate dehydrate ($C_4H_{10}O_6Zn$; ≥99.0 %; CAS Number: 5970-45-6) salts were used to synthesize binary CuO– ZnO films. Cadmium acetate dehydrate ($C_4H_{10}CdO_6$; ≥98.0 %; CAS Number: 5743-04-4) salt was used to obtain Cd^{2+} ion. All chemicals used in this study without further purification were obtained from Sigma-Aldrich.

40 mL of 0.1 M $Cl_2CuH_4O_2$ salt and 60 mL of 0.1 M $C_4H_{10}O_6Zn$ salt were dissolved in 100 mL of distilled water to obtain a Cu^{2+}-Zn^{2+} solution. The solution was stirred for 5 min to make it more homogeneous and transparent. The pH of the reaction bath was optimized by adding NH_4OH (Company Sigma-Aldrich), and then the temperature of the growth solution was raised to 85 °C and kept constant at this temperature. Glass substrates were first immersed in Cu^{2+}-Zn^{2+} aqueous solution and then in pure water to remove ions weakly bound to the substrate material. The drying process was then applied in an air environment. All these procedures were performed for 20 s. The dipping, rinsing, and drying processes were repeated 30 times to obtain the desired thickness of the CuO–ZnO NC films. To investigate the effect of Cd^{2+} ions on the physical properties of binary CuO–ZnO NC films, different percentages (1.0 % and 2.0 %) of Cd^{2+} were added to the Cu^{2+}-Zn^{2+} solution. The above loop operations were repeated. The produced un-doped CuO–ZnO NC and Cd-doped binary CuO–ZnO NC films were annealed in an oven at 250 °C for 45 min.

The microstructure and surface morphologies of all produced CuO–ZnO binary NC films were examined by field emission scanning electron microscopy (FE-SEM) using a Zeiss Model: GEMINI 500 (Accelerating Voltage: 0.02–30.0 kV) and atomic force microscopy (AFM) using a Park System XE7-Nanoindentasyon (High-performance DSP: 600 MHz with 4800 MIPS). Chemical elemental analysis and mapping were performed using an energy-dispersive X-ray spectrometer (EDX) connected to the FE-SEM unit. X-ray diffraction (XRD) measurements of binary composite films were performed using an X-ray diffractometer (Bruker D8 Advance, using CuKα (λ = 1.518 Å), operated at 40 kV). The AEP Technology NanoMap 500 LS 3D profilometer device was used to determine the thickness values of the NC films by taking measurements from different points. Optical properties, such as optical transmission and band gap, were investigated using a Jasco V-670 UV–Vis spectrophotometer.

The chemical bonding properties of CuO– ZnO binary NC films were examined by Fourier transform-infrared and Raman spectroscopy methods using a PerkinElmer 400 FT-IR Spectrometer Spotlight 400 Imaging System and WITec Alpha M+ (532 nm, 785 nm), respectively. Electrical measurements (I-V) were accomplished via a computer-controlled Agilent B2912A SMU at room temperature and in the dark. The transfer length method (TLM) was used to determine the electrical resistivity. Contact patterns were created using thermally evaporated high-purity gold. Controlling the SMU and data processing was performed using our VEE Pro-based SeCLaS software [32,33].

3. Results and discussion

3.1. Morphological properties

FE-SEM imaging was performed at different magnifications for surface morphological imaging of Cd-doped and un-doped CuO–ZnO binary NC films. Fig. 1a shows the FE-SEM images of the un-doped CuO–ZnO binary NC thin film, and Fig. 1b and c shows the images of 1.0 % Cd-doped and 2.0 % Cd-doped films, respectively. In general, rod-shaped ZnO nanostructures with hexagonal cross-sections were obtained in all NC films [34]. Visualizations of these structures are marked in blue on the figures. CuO structures are located at the bottom of the thin film but can be observed among the ZnO structures. CuO nanostructures are observed as structures with a flower-like appearance, similar to candocks in nature [35]. These structures can be seen more clearly in the close-up images (middle) and are highlighted in red. It was observed that doping did not cause a significant change in the CuO nanostructure, whereas 2.0 % Cd doping caused a significant change in the morphology of the ZnO structure. It is observed that doping affects the nucleation and crystallization processes.

In Fig. 1c, the morphological change is noticeable at the ends of the rod-shaped ZnO nanostructures. Studies reporting the change in the tip parts of ZnO nanostructures due to the doping process can be found in the literature [36]. In the cross-sections of the ZnO structures of the CuO–ZnO/2.0%Cd film, the distortion of the hexagonal form increases and the rod length decreases. The film thicknesses obtained from profilometer measurements are 0.41 μm, 0.38 μm, and 0.29 μm for CuO–ZnO, CuO–ZnO/1.0%Cd, and CuO–ZnO/2.0%Cd NC films, respectively. In particular, the morphological change in the 2.0 % Cd contribution is compatible with the larger change in film thickness.

In addition, EDX analysis was performed for CuO–ZnO and CuO–ZnO/2.0%Cd thin films. Both elemental analysis and mapping were performed on the NC films. Thus, the placement of the elements in the NC film morphology was visualized. EDX results are shown in Fig. 2a and b for CuO–ZnO and CuO–ZnO/2.0%Cd binary NC films, respectively. Cu, O, and Zn peaks are observed for both films, but an additional Cd peak is observed in Fig. 2b. The weight percentages of the elements are included in the table embedded in the figure. Observation of all elements in the structure of the thin films shows that the film production and doping processes have been successfully carried out. In the larger general mapping image in Fig. 2b, the increase in the cyan tone on the surface is evident, and in the mapping image representing only Cd, the cyan tone is more intense at the ends of the rod structure. This may support the contention that Cd is the source of the distortion in the hexagonal section at the rod ends of the ZnO structure, which is also mentioned in the FE-SEM images.

The surface properties of the CuO–ZnO binary NC films were further investigated using AFM topography. Fig. 3 shows the 2D and 3D topographies and some obtained parameters. Fig. 3a shows the results for the un-doped ZnO– CuO film, and Fig. 3b and c shows the results for the 1.0 % Cd-doped and 2.0 % Cd-doped films, respectively.

The AFM images demonstrate the existence of crystalline grains that decrease in size as the Cd percentage increases. This confirms the nanocrystalline structure of the films, as evidenced by the decreasing crystallite size values with increasing Cd percentage obtained from the XRD data [37,38]. The AFM images, both 2D and 3D, demonstrate that the grain size decreases as the film thickness decreases. This result is in agreement with the reduction in crystallite size observed in the XRD analysis. The reduction in film thickness is responsible for the decrease in local grain size [39]. The roughness parameters of the composite thin films, peak-to-valley peak height (Rpv), root mean square roughness (Rq), average roughness (Ra), maximum peak height (Rz), skewness (Rsk), and kurtosis (Rku), are integrated in the figure as a table. These

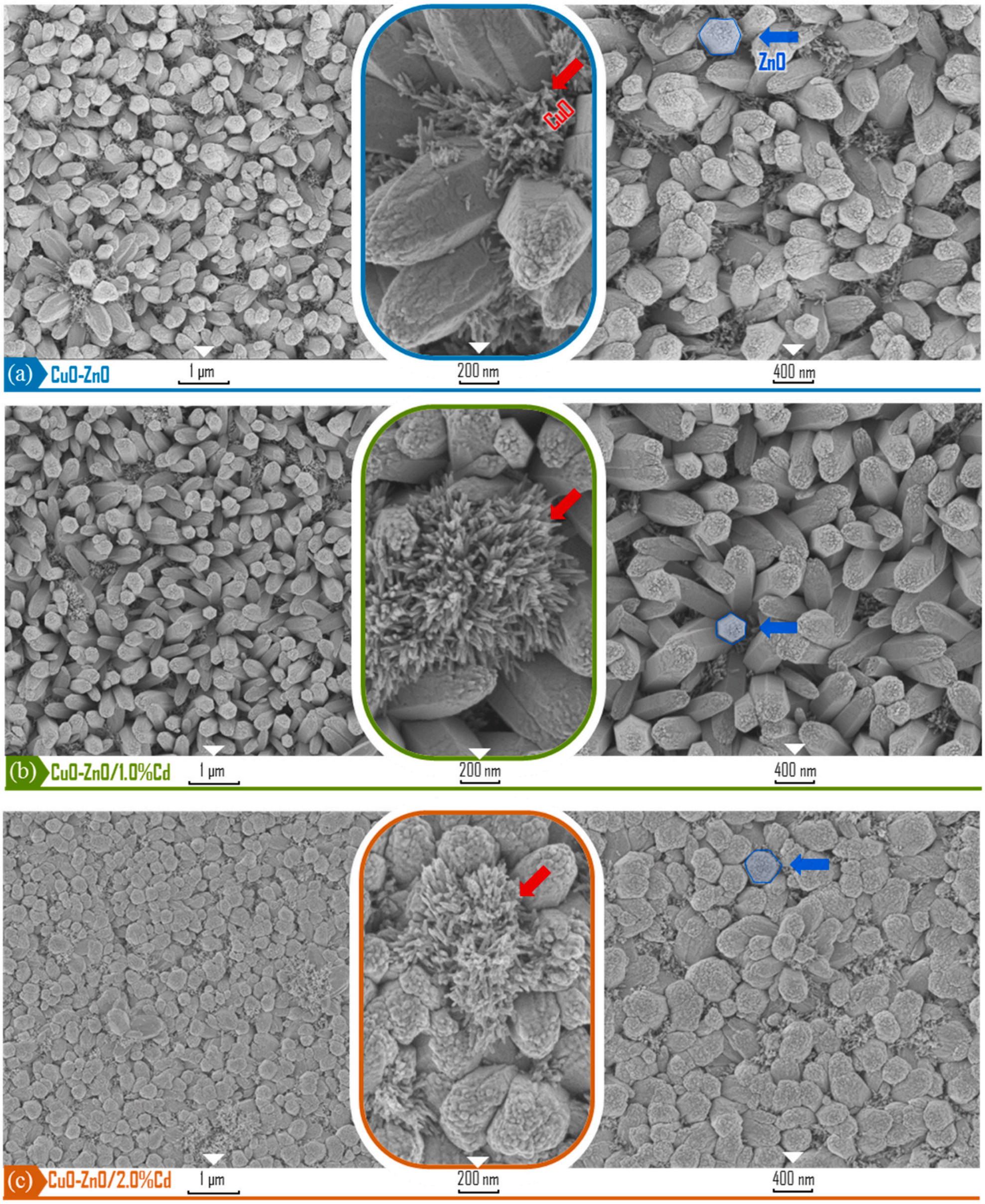

Fig. 1. FE-SEM surface images of a) undoped binary CuO-ZnO, b) CuO-ZnO/1.0%Cd, and c) CuO-ZnO/2.0%Cd binary NC thin films.

parameters provide important clues about the roughness of the thin film surfaces. Surface roughness affects the progression of adsorption and desorption processes on the film surface [40]. For example, Rku is a measure of the sharpness of the surface profile, and Rsk provides information about the troughs (negative values) and peaks (positive values) [41]. While Rsk is positive for the CuO– ZnO film, it is negative for the other two Cd-doped films. It was found that Rq decreased from 87.381 nm to 72.733 nm with increasing Cd content from 0 to 2.0. That is, the Rq value decreases with Cd doping. The decrease in Rq with increasing Cd content is attributed to a reduction in grain size. This suggests that Cd doping can effectively refine the surface of Cd-doped CuO-ZnO films [42]. Similarly, the Ra value decreases from ~70 nm for the CuO– ZnO film to ~60 nm for the CuO– ZnO/1.0%Cd film and decreases to ~55 nm for the CuO– ZnO/2.0%Cd film. In the FE-SEM analysis, it was observed that ZnO nanotips transformed into a repressed form with Cd doping, and the hexagonal cross-section was distorted. The results can be associated with these values and support each other. 2D and 3D topographies also clearly show that surface roughness is affected by doping.

3.2. *Structural properties*

XRD images of binary CuO– ZnO binary NC films synthesized on glass with different Cd^{2+} contents (1.0 and 2.0 %) are shown in Fig. 4. The diffraction lines reveal the entity of CuO and ZnO phases, which is verified by the observed 2θ values at 32.26° (110), 34.92° $(\bar{1}11)$, 48.04° $(\bar{2}02)$, 68.50° (220) and 73.03° (311) for monoclinic structure CuO (JCPDS No. 05-0661) and 2θ values at 34.92° (002), 36.76° (101), 48.04° (102), 57.05° (110), 63.33° (103) and 73.03° (004) for hexagonal structure ZnO (JCPDS No. 36-1451) [43,44]. In Fig. 4, an intense diffraction peak was observed at 34.92°, which corresponds to the $(\bar{1}11)$ plane of CuO and the (002) plane of ZnO. The intense and sharp peak lines indicate that the produced binary NC films have a highly crystalline structure. XRD analysis confirms the presence of Cd in the CuO-ZnO composite lattice. Due to the increasing Cd^{2+} percentages in the reaction bath, CuO $(\bar{1}11)$ and ZnO (002) peak intensities first increased and then decreased. Peak intensities are given in Table 1. This change in peak intensities may be due to the change in the CuO–ZnO lattice

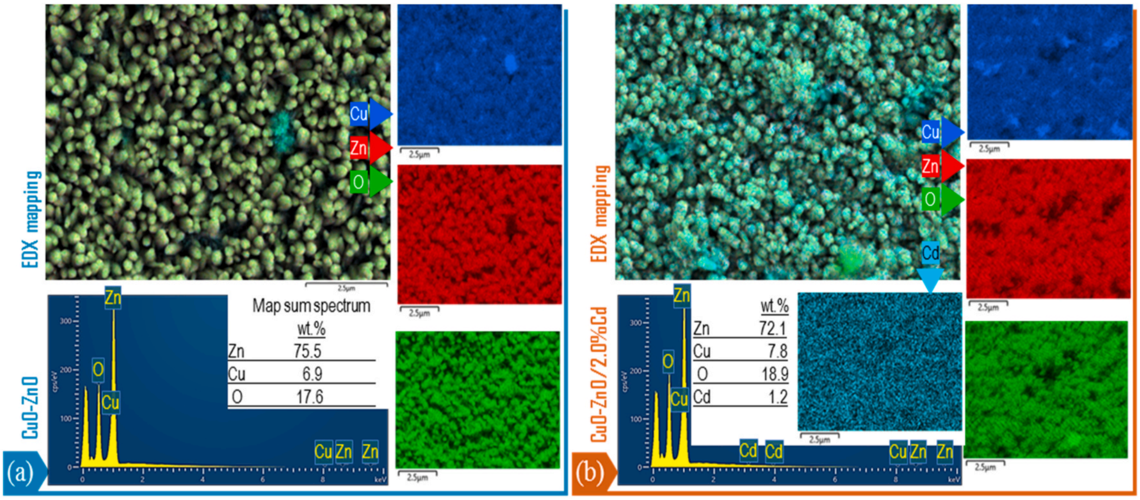

Fig. 2. EDX analysis and EDX-mapping images of a) undoped binary CuO-ZnO and b) 2.0 % Cd-doped binary NC thin films.

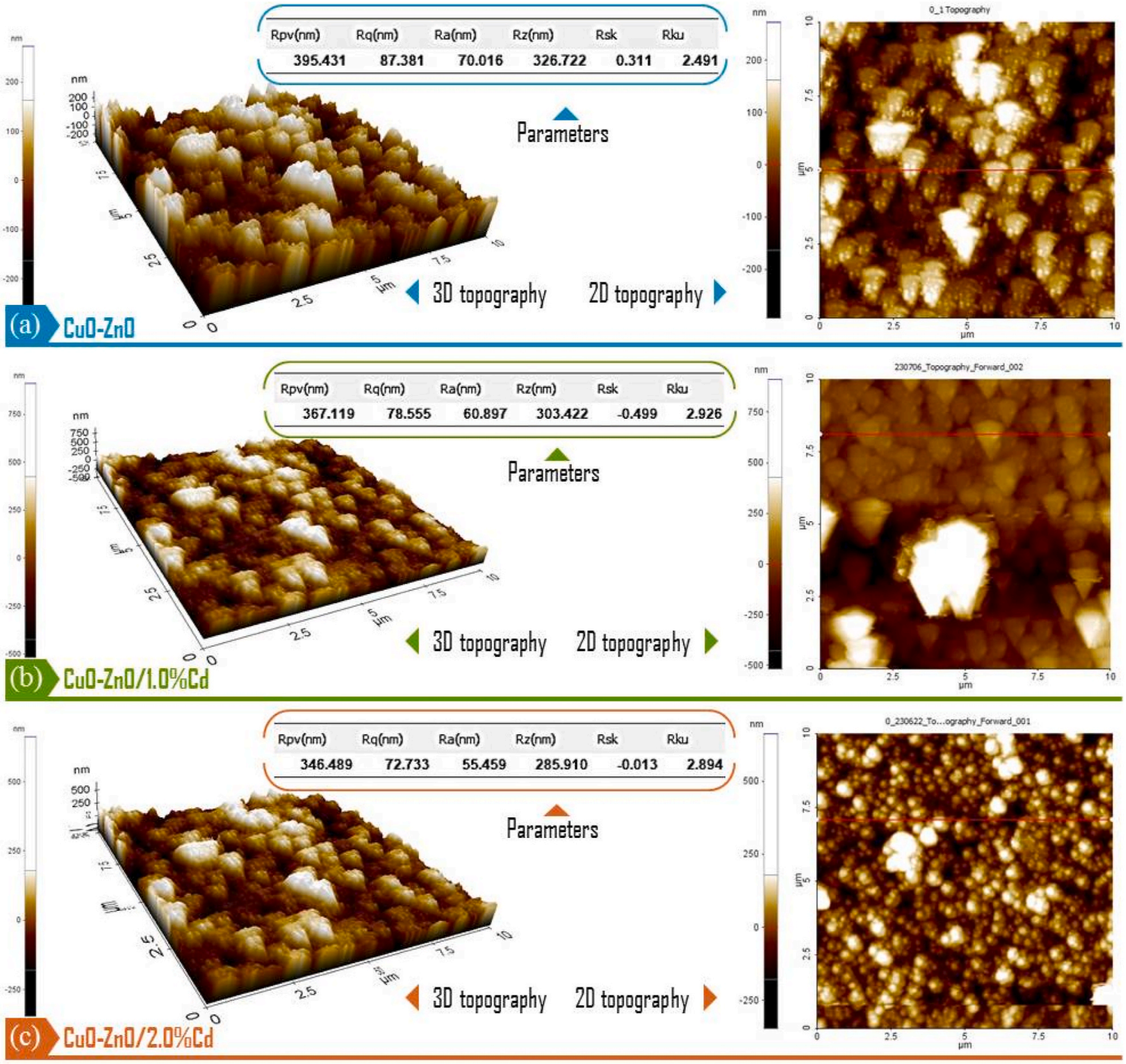

Fig. 3. 2D and 3D surface topographies and roughness parameters obtained by AFM for a) CuO-ZnO, b) CuO-ZnO/1.0%Cd, and c) CuO-ZnO/2.0%Cd.

structure due to the different ionic radii of Cu^{2+}, Zn^{2+}, and Cd^{2+} with the addition of Cd^{2+} to the solution ($Cu^{2+} = 0.57$ Å, $Zn^{2+} = 0.60$ Å, and $Cd^{2+} = 0.78$ Å; for 4-coordination number) [45,46].

The average crystallite size (D) of the un-doped and Cd^{2+}-doped binary CuO–ZnO NC films was calculated using Scherrer's rule [47].

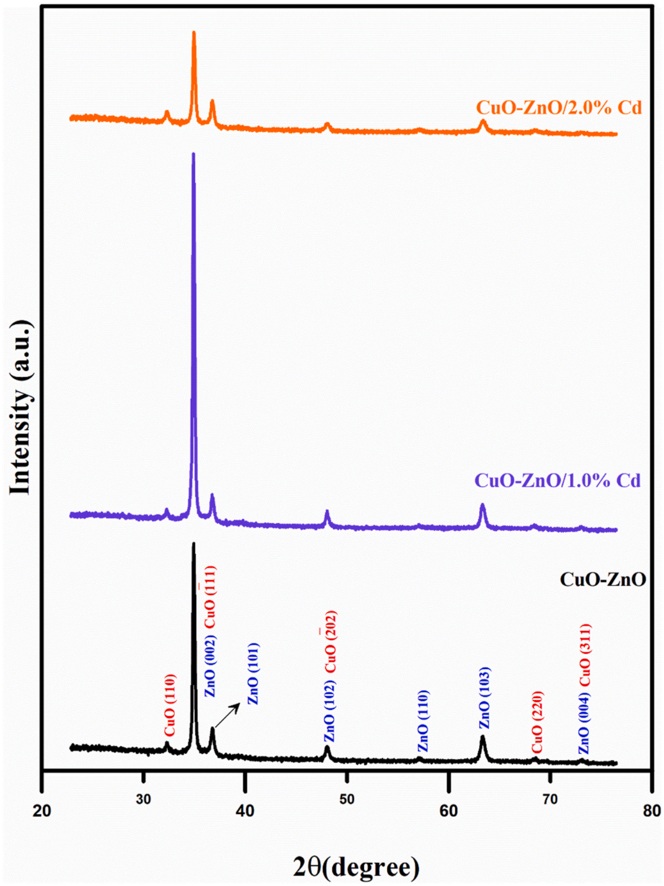

Fig. 4. XRD patterns of binary CuO-ZnO NC films deposited at two different Cd molar concentrations.

Table 1
Relative peak intensity, crystallite size and film thickness values of CuO-ZnO binary NC films as a function of Cd^{2+} concentration in the growth solutions of the SILAR process.

Sample Name	Relative Peak Intensity (cps) CuO ($\bar{1}$**11**)/ZnO (002)	Crystallite Size (nm)	Film Thickness (μm)
CuO-ZnO	4481	25.91	0.41
CuO-ZnO/1.0 % Cd	7795	22.68	0.38
CuO-ZnO/2.0 % Cd	1915	19.23	0.29

$$D = \frac{0.94\lambda}{\beta \cos \theta} \tag{1}$$

β, λ, and θ in the equation are the full width at half maximum, X-ray wavelength, and Bragg angle, respectively. The average D values obtained are given in Table 1. As shown in Table 1, as the Cd^{2+} concentration in the solution bath increases, the D values of the CuO–ZnO binary NC films decrease. This change in D can be attributed to the presence of Cd^{2+}, which can regulate the pattern and size of crystallites by affecting their growth and nucleation. Furthermore, this decrease in D can be ascribed to the close-packed crystal structure of the composite materials [48,49].

3.3. FTIR and RAMAN

FT-IR and Raman spectroscopy methods were used to examine the different vibration modes and Raman active phonon modes of the fabricated CuO– ZnO binary NC films. Here, CuO has a monoclinic structure, and according to group theory, they have 12 zone-center optical phonon modes [50–52]. Nine of these modes are IR active modes ($4A_u$+$5B_u$) three of them are acoustic, and six are IR active modes. The remaining three modes are Raman mode ($1A_g$+$2B_g$) [53,54]. Similarly, ZnO has six optical modes ($1A_1$+$2B_1$+$1E_1$+$2E_2$), in which $2B_1$ is a silent mode, optical modes E_1 and A_1 are active modes, and $2E_2$ is an infrared Raman active mode [55,56]. In addition, the E_1 and A_1 active modes are divided into two phonons (Longitudinal and transverse optical phonons (LO and TO)). In the same way, nonpolar phonon modes are divided into two frequencies ($E_{2\ (high)}$ and $E_{2\ (low)}$), and, these active modes are interrelated with oxygen atom modes and the Zn sub-lattice, respectively [57–59]. Raman scattering occurs along the ZnO nanorods; thus, only $E_{2\ (high)}$ and A_1 LO are Raman active [56,60].

Fig. 5 shows the recorded FTIR spectra of the Cd-doped (1.0 % and 2.0 %) and undoped binary CuO– ZnO samples to determine their structural confirmations. The FTIR spectra of the prepared binary CuO–ZnO samples were recorded in the wavenumber range 400–4000 cm^{-1} and as shown in Fig. 5, indicated the presence of many vibrational modes.

Metal-oxide materials such as ZnO and CuO exhibit strong absorption bands in the higher frequency region (fingerprint region, below 1000 cm^{-1}) due to the stretching modes of Cu and Zn to oxygen bonds. Therefore, strong peaks between 455 and 852 cm^{-1} can be assigned to the overlap of the typical stretching vibration modes of the Cu–O and Zn–O bonds [20,51,56,61,62]. In the functional group regime, the peaks can be ascribed to residual precursors, organic contamination, and atmospheric CO_2 on the metallic cations [56,61,63].

Fig. 6 shows the Raman spectra of the un-doped and Cd-doped CuO–ZnO binary NC films. The co-excited CuO and ZnO Raman modes in the Raman spectra confirm the creation of binary CuO–ZnO films. In addition, the peak values are almost constant for all films, and no peak observed related to the dopant atom-based compounds. This confirms that Cd atoms have been successfully located in the host CuO/ZnO matrix at cationic sites. These results were also confirmed via XRD analysis.

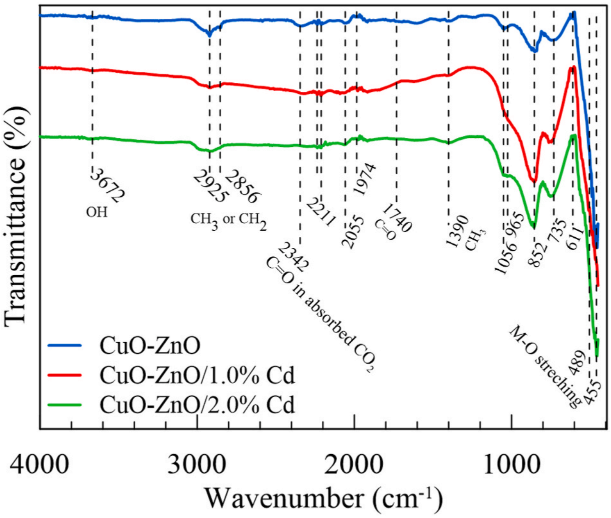

Fig. 5. FTIR spectrum of Cd-doped (1.0 % and 2.0 %) and un-doped CuO-ZnO binary samples. ZnO and CuO both exhibit absorption bands in the high-frequency region stretching modes of metal-oxide materials.

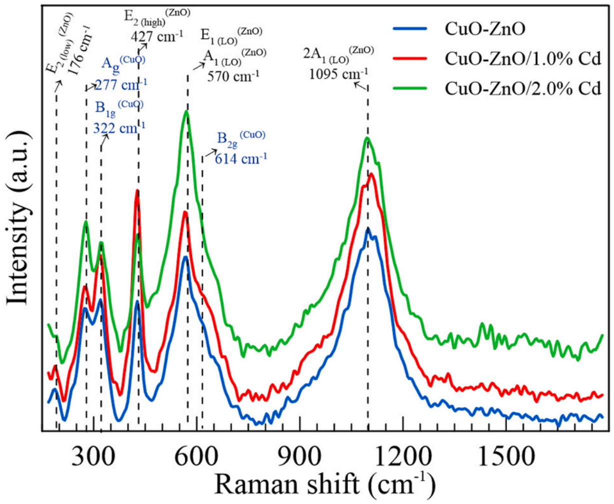

Fig. 6. Raman spectra of Cd-doped (1.0 % and 2.0 %) and un-doped CuO-ZnO binary samples using using the 632 nm excitation.

3.4. Optical properties

The optical properties of the fabricated CuO–ZnO NC binary thin films were examined using UV–Vis. The optical bandgap energy is a significant phenomenon in the optoelectronic usability of thin film materials and is mainly dependent on the film structure and morphology. The bandgap energy values of the CuO– ZnO binary NC films were estimated from Tauc's relationship (Eq. (2)).

$$\alpha h\nu = C\left(h\nu - E_g\right)^{1/2} \tag{2}$$

Where hυ is the photon energy, and α is the absorption coefficient. The $(\alpha h\upsilon)^2$ vs (hυ) plotting of bare and Cd-substituted CuO– ZnO binary NC films are shown in Fig. 7.

The estimated bandgap value for the bare CuO– ZnO NC film is approximately 2.26 eV, which increases to 2.77 eV after doping with Cd in the growth bath. These band gap values have been supported by other researchers [64–66]. The increase in optical bandgap energy corresponds to the blue shift in the absorption edge of the Cd-substituted binary CuO–ZnO NCs. The Cd-substituted binary CuO–ZnO NC thin films reveal both maximal optical bandgap and high transmittance among the fabricated thin film materials.

The alteration in the optical energy gap may be due to the change in particle size, structure, and distribution with increasing Cd content in the growth bath. An increase in the Cd content leads to a change in the intragap impurity bands [67]. In addition, the widening of the optical bandgap energy may be due to the combined effect of quantum size and Burstein –Moss effects [68]. Meanwhile, a similar change in the optical bandgap with metal doping is ascribed to the shrinkage of the Eg of the host metal oxide materials due to the interactions between the "sp-d" formed band electrons and the "d" localized electrons of the dopant material [69,70].

In this research, small doping concentrations (1.0 % and 2.0 %) were chosen to achieve positive physical enhancements, which can easily lead to electron density changes because of the limit of solid solubility in the solution-based growth bath. Thus the optical band gap distinctly increased and the conductivity slightly decreased due to the extended localization arising from the crystallinity quality and changed impurity scattering at lower dopants [71]. Furthermore, the Eg change is fundamentally due to the alteration in CuO-ZnO grain boundaries, the recuperation of crystalline characteristics, and structural defects in the samples [72].

The absorption edge of the fabricated thin film materials changes with a change in the dopant concentration associated with a change in the carrier concentration in the conduction band according to the Burstein-Moss effect [73,74]. This demonstrates the shift in the Fermi level in the conduction band owing to changed charge carriers, which influence the Eg values. Thus, the existence of Cd-dopants in the samples influences the concentration and position of the carrier, which leads to a widening of the bandgap energy, as we mentioned above.

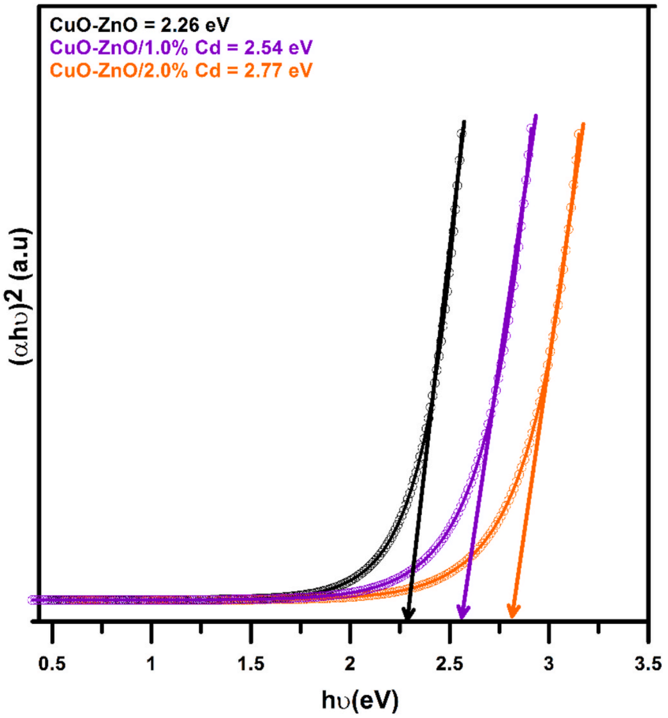

Fig. 7. The $(\alpha h\upsilon)^2$ vs (hυ) plotting of bare and Cd-substituted CuO-ZnO binary NC films. The estimated optical bandgap value for the bare CuO-ZnO NC film is about 2.26 eV, which increases to 2.77 eV after being doped with Cd in the growth bath solution. The increase in optical bandgap energy corresponds to the blue shift in the absorption edge of the Cd-substituted CuO-ZnO binary NCs.

The transmittance spectra of the fabricated CuO–ZnO binary NC films are shown in Fig. 8. It was observed that the bare CuO–ZnO NC films' optical transmittance values were enhanced compared to Cd-substituted samples, and the maximum rate was obtained to be approximately 70.0 % related to 2.0 % Cd substitution.

By tailoring the bandgap energy, the conductivity properties of these nanostructured metal-oxide-based materials can be adjusted to design various devices, such as transistors, diodes, and other digital equipment. The wider optical bandgap energy is exclusively significant for allowing designed materials that utilize them to operate at much higher temperature conditions [75]. This qualification is indispensable for the design of optoelectronic devices. The obtained outcome could be used to enhance the impression of photovoltaic devices.

3.5. Electrical properties

Fig. 9 shows the current– voltage (I-V) measurement results of Cd-doped and un-doped CuO– ZnO binary thin films within the range of −5 to 5 V at room temperature. All films exhibit ohmic behavior and indicate that conductivity depends on the Cd-doping level. When determining the resistance value of such a thin film structure, considering the effective transfer length (L_{eff}) and specific contact resistance (ρ_c) rather than the properties of the bulk material gives more accurate results.

The resistivity values of films can be precisely determined by the transfer length method (TLM) by their nature. According to this method, there are 3 contacts with distances l_1 and l_2 between each other (see inset

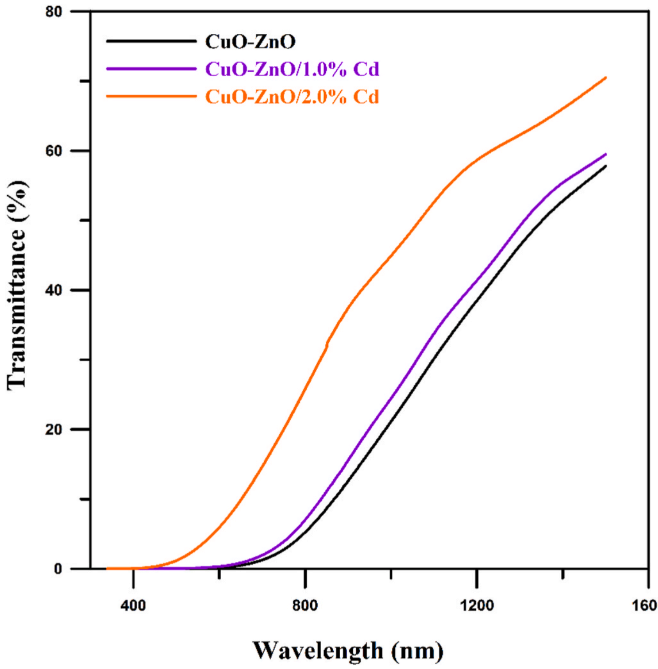

Fig. 8. Transmittance spectra of fabricated binary CuO-ZnO NC films. Bare CuO-ZnO NC films' optical transmittance values are enhanced as compared to Cd-substituted samples and the maximum rate has been obtained to be here about 70.0 % related to 2.0 % Cd substitution.

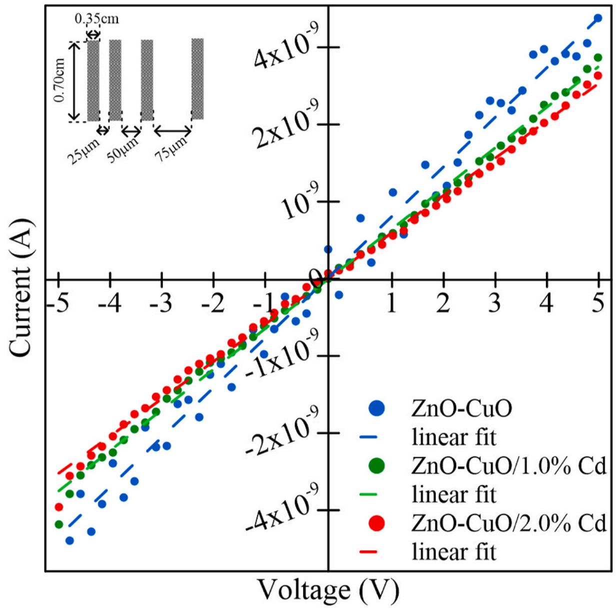

Fig. 9. I-V characteristics and linear fits of Cd-doped (1.0 % and 2.0 %) and un-doped CuO-ZnO binary thin films. The dc resistivity values decreased with the Cd content. Inset shows TLM contact pattern.

in Fig. 9.) and take into the account the current crowding phenomenon [76–78]. The relationship between the total contact resistance (R_C) and the transfer length (L_T) can be expressed as follows [78].

$$R_c = \frac{R_{Sk} L_T}{w} \coth\left(d/_{L_T} \right) \tag{3}$$

and

$$L_T = \sqrt{\frac{\rho_c}{R_{Sk}}} \tag{4}$$

Here, w is the width of the contact, d is the length of the contact, and R_{Sk} is the modified sheet resistance under the contact. In addition, contact resistance can be written simply as follows, depending on the specific contact resistance (ρ_c) [77].

$$R_c = \frac{\rho_c}{L_T d} \coth\left(w/_{L_{eff}} \right) \tag{5}$$

In addition, assuming that the effective transfer distance is much smaller than the width of contact ($w \gtrsim 2L_{eff}$), the total resistance (R_T) is given by

$$R_T = \frac{2R_{Sk} L_T}{w} + \frac{R_{Sh} l}{w} \tag{6}$$

where R_{Sh} is the sheet resistance outside the contact region.

In addition, R_T versus d plots (Fig. 10.) can be used to calculate of R_{Sh}, R_C, and L_T for the $2R_{SK} = R_{SH}$ condition [76,77]. Also, for the condition $L_x \neq L_T$, contact end resistance (R_{end}) is written as [77]

$$R_{end} = \frac{\rho_c}{L_T w} \frac{1}{sinh\left(d/_{L_T} \right)} \tag{7}$$

The lowest specific contact resistivity of 2.976x10^{6} Ω□ was achieved by un-doped binary CuO–ZnO thin films and adding Cd slightly increased the specific contact resistivity values to 22.176x10^{6} Ω□ for CuO–ZnO/2.0 % Cd binary films (Fig. 11a). This increase in contact resistivity can be explained by the effect of many parameters such as particle size, impurities, grain boundaries, and surface roughness. Similarly, the transfer length and contact resistance increased with the Cd content (Fig. 11(b–c)).

The conductivity properties of nanostructured thin film materials depend on various parameters, such as structural defects, particle morphology, and growing conditions. The same change in contact resistance of doped thin films has been recorded by several groups independently of the fabrication methods used during the preparation of samples [79,80]. Regarding conductivity performances, oxygen vacancies play a significant role, as their increment influences the resistance of CuO–ZnO binary structures. When CuO–ZnO binary films are

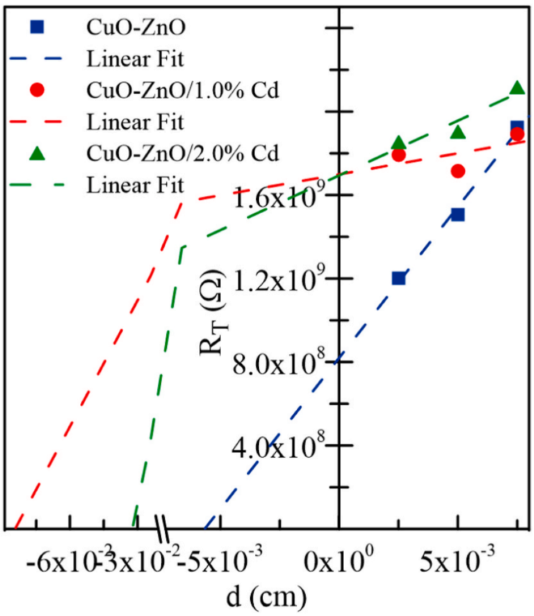

Fig. 10. Plot of total resistance as a function of pad distance to obtain transfer length and contact resistance.

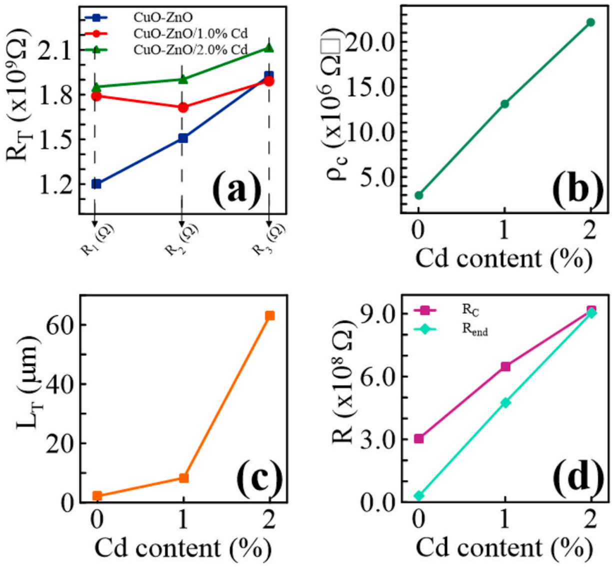

Fig. 11. Total resistance (R_T) (a) and plot of contact parameters ρ_c (b), L_T (c), R_{end} and R_C (d) as a function of Cd content (%).

doped with Cd elements, doped Cd atoms tend to accumulate in the grain boundaries, contributing to the oxidation process.

This decreasement in conductivity is additionally owing to the aggregation of charge carrier capture sites at the grain boundaries, which diminishes carrier mobility in the CuO-ZnO matrix. Meanwhile, the conductivity efficiency of thin film samples in nano-scale depend on film thickness. The sample conductivity decreases with increasing film thickness (with growing Cd content) was ascribed to the increment in scattering efficiency like phonon scattering and ionized impurity scattering. A similar justification for rising the R_s that these extra Cd ions cannot receive convenient lattice sites to ensure free carriers, which leads to an increment in defect states that raise the R_s value [81–83].

4. Conclusion

Semiconductor structures and transparent Cd-doped CuO–ZnO binary NC thin films were fabricated. The influence of Cd-doping concentrations on the surface morphological, structural, optical, and electrical characteristics was performed. The co-excited CuO and ZnO Raman modes in the Raman spectra confirm the creation of binary CuO–ZnO films. These results were also confirmed via XRD analyzes The Cd-doping process led to optical bandgap widening of the bare CuO–ZnO binary NC thin film from 2.26 to 2.77 eV. In addition, in the films, an important change in the optical transmittance was recorded. The lowest specific contact resistivity of 2.976x10^6 Ω□ was achieved by un-doped binary CuO–ZnO thin films and adding Cd slightly increased the specific contact resistivity values to 22.176x10^6 Ω□ for 2.0 % Cd-doped sample. The primary physical properties of CuO-ZnO binary oxides have been enhanced with a transition metal Cd doping to apply them as a candidate optoelectronic system. The obtained outcomes can be explained by the p-n heterojunction interface and optoelectronic material characteristics of CuO-ZnO binary oxide structures.

CRediT authorship contribution statement

Halimenur Satılmış: Investigation, Resources. **Merve Acar:** Investigation, Resources. **Raşit Aydın:** Data curation, Investigation, Methodology, Supervision, Writing – review & editing. **Abdullah Akkaya:** Data curation, Investigation, Methodology, Writing – review & editing. **Osman Kahveci:** Data curation, Investigation, Methodology, Writing – review & editing. **Bünyamin Şahin:** Data curation, Investigation, Methodology, Resources, Writing – review & editing. **Enise Ayyıldız:** Investigation, Methodology, Resources, Writing – review & editing.

Declaration of competing interest

The authors declare that they have no known competing financial interests or personal relationships that could have appeared to influence the work reported in this paper.

Data availability

No data was used for the research described in the article.

Acknowledgments

This work was supported by The Scientific and Technological Research Council of Türkiye (TUBITAK) 2209-A - Research Project Support Programme for Undergraduate Students (Application/Project No: 1919B012216060).

References

[1] H.A. Abo-Mosallam, M.M. Farag, J. Mater. Sci. Mater. Electron. 34 (2023) 602.
[2] A.U. Hasanah, P.L. Gareso, N. Rauf, D. Tahir, ChemBioEng Rev. 10 (2023) 698–710.
[3] A.U. Ammar, M. Stan, A. Popa, D. Toloman, S. Macavei, C. Leostean, A. Ciorita, E. Erdem, A.M. Rostas, J. Energy Storage 72 (2023) 108599.
[4] H. Notohara, K. Urita, I. Moriguchi, Acs Appl Mater Inter 15 (2023) 30600–30605.
[5] Y. Wang, J. Liu, C. Su, L. Jin, J. Sol. Gel Sci. Technol. 103 (2022) 367–377.
[6] J. Aslam, Y. Wang, Nanomaterials-Basel 13 (2023) 296.
[7] Y.-K. Syue, K.-C. Hsu, T.-H. Fang, C.-I. Lee, C.-J. Shih, Ceram. Int. 48 (2022) 12585–12591.
[8] L. Wu, G. Jiang, X. Wang, Y. Wang, Y. Zhou, Z. Wu, J. Colloid Interface Sci. 622 (2022) 62–74.
[9] K. Qi, B. Cheng, J. Yu, W. Ho, J. Alloys Compd. 727 (2017) 792–820.
[10] Z. Jiang, B. Liu, L. Yu, Y. Tong, M. Yan, R. Zhang, W. Han, Y. Hao, L. Shangguan, S. Zhang, W. Li, J. Alloys Compd. 956 (2023) 170316.
[11] I. Hussain, N.B. Singh, A. Singh, H. Singh, S.C. Singh, Biotechnol. Lett. 38 (2016) 545–560.
[12] A.P. Ingle, N. Duran, M. Rai, Appl. Microbiol. Biotechnol. 98 (2014) 1001–1009.
[13] E. Morrison, D. Gutiérrez-Tauste, C. Domingo, E. Vigil, J.A. Ayllón, Thin Solid Films 517 (2009) 5621–5624.
[14] L. Jiang, S. Tu, K. Xue, H. Yu, X. Hou, Ceram. Int. 47 (2021) 7528–7538.
[15] R.A. Basit, Z. Abbasi, M. Hafeez, P. Ahmad, J. Khan, M.U. Khandaker, K.S. Al-Mugren, A. Khalid, Crystals 13 (2023) 281.
[16] D. Chua, S.B. Kim, K. Li, R. Gordon, ACS Appl. Energy Mater. 2 (2019) 7750–7756.
[17] I. Sanusi, C.B. Almquist, Catalysts 13 (2023) 1203.
[18] R.S. Pugina, D.L. da Silva, A. Riul, M.L. da Silva-Neto, A.S.L. Gomes, J.M.A. Caiut, Polymer 241 (2022) 124541.
[19] K. Sahu, A. Bisht, S.A. Khan, A. Pandey, S. Mohapatra, Ceram. Int. 46 (2020) 7499–7509.
[20] O. Kahveci, A. Akkaya, E. Yücel, R. Aydın, B. Şahin, Ceram. Int. 49 (2023) 16458–16466.
[21] G. Yergaliuly, B. Soltabayev, S. Kalybekkyzy, Z. Bakenov, A. Mentbayeva, Sci Rep-Uk 12 (2022) 851.
[22] A. Taşdemir, N. Akman, A. Akkaya, R. Aydın, B. Şahin, Ceram. Int. 48 (2022) 10164–10173.
[23] S.K. Shinde, G.S. Ghodake, V.J. Fulari, D.Y. Kim, J. Ind. Eng. Chem. 52 (2017) 12–17.
[24] P. Chaudhary, A. Agrwal, D.K. Sharma, V. Kumar, J. Sol. Gel Sci. Technol. 104 (2022) 425–433.
[25] L. Guo, W. Liu, C. Wang, ACS Appl. Nano Mater. 6 (2023) 7830–7840.
[26] F. Iram, G.M. Mustafa, G. Ali, H. Ahmad, S.M. Ramay, Z. Iqbal, S. Atiq, J. Energy Storage 73 (2023) 108829.
[27] I.M.P. Silva, G. Byzynski, C. Ribeiro, E. Longo, J. Mol. Catal. Chem. 417 (2016) 89–100.
[28] A. Pramothkumar, N. Senthilkumar, R.M. Jenila, M. Durairaj, T.C.S. Girisun, I. V. Potheher, J. Alloys Compd. 878 (2021) 160332.
[29] A.A.A. Al-Mushki, A.A.A. Ahmed, A.M. Abdulwahab, B.A. Al-Asbahi, J.M. A. Abduljalil, F.A.A. Saad, N.M. Al-Hada, S.M.H. Qaid, H.M. Ghaithan, Appl. Phys. A 128 (2022) 279.
[30] A.A.A. Al-Mushki, A.A.A. Ahmed, A.M. Abdulwahab, S.A.S. Qaid, N.S. Alzayed, M. Shahabuddin, J.M.A. Abduljalil, F.A.A. Saad, Sci Rep-Uk 13 (2023) 9021.
[31] R. Aydin, B. Sahin, Ceram. Int. 44 (2018) 22249–22254.
[32] A. Akkaya, E. Ayyıldız, J. Circ. Syst. Comput. 29 (2020) 2050215.
[33] A. Akkaya, E. Ayyıldız, MAPAN 35 (2020) 343–350.
[34] C.M. Mbulanga, W.E. Goosen, R. Betz, J.R. Botha, Appl. Phys. A 126 (2020) 180.
[35] G. Fan, F. Li, Chem. Eng. J. 167 (2011) 388–396.
[36] R. Yousefi, M.R. Muhamad, A.K. Zak, Thin Solid Films 518 (2010) 5971–5977.

[37] M. El-Hagary, S.H. Moustafa, H. Hashem, E.R. Shaaban, M. Emam-Ismail, J. Am. Ceram. Soc. 102 (2019) 4737–4747.
[38] G.A. Ali, M. Emam-Ismail, M. El-Hagary, E.R. Shaaban, S.H. Moustafa, M.I. Amer, H. Shaban, Opt. Mater. 119 (2021) 111312.
[39] M. Emam-Ismail, M. El-Hagary, H.M. El-Sherif, A.M. El-Naggar, M.M. El-Nahass, Opt. Mater. 112 (2021) 110763.
[40] K.N.D. Bandara, K.M.D.C. Jayathilaka, D.P. Dissanayake, J.K.D.S. Jayanetti, Appl. Surf. Sci. 561 (2021) 150020.
[41] C.-W. Chan, L. Carson, G.C. Smith, A. Morelli, S. Lee, Appl. Surf. Sci. 404 (2017) 67–81.
[42] M. Emam-Ismail, M. El-Hagary, E.R. Shaaban, S.H. Moustafa, G.M.A. Gad, Ceram. Int. 45 (2019) 8380–8387.
[43] N.T.T. Nguyen, L.M. Nguyen, T.T.T. Nguyen, N.H. Nguyen, D.H. Nguyen, D.T. C. Nguyen, T.V. Tran, J. Environ. Manag. 326 (2023) 116746.
[44] L.A. Kolahalam, K.R.S. Prasad, P.M. Krishna, N. Supraja, S. Shanmugan, Heliyon 8 (2022) e09726.
[45] R. Shannon, Acta Crystallogr. A 32 (1976) 751–767.
[46] H. Bishwakarma, A. Kumar Das, P. Kumar, P. Kumar Singh, M.M. Awad, J. Taibah Univ. Sci. 17 (2023) 2188017.
[47] B. Sahin, R. Aydin, Phys. B Condens. Matter 541 (2018) 95–102.
[48] S. Ouir, H. Lachenani, F. Boudeffar, A. Bouaoua, H. Cheraga, F. Zermane, Z. Benmaamar, N. Gabouze, Appl. Phys. A 129 (2022) 10.
[49] K. Mubeen, A. Irshad, A. Safeen, U. Aziz, K. Safeen, T. Ghani, K. Khan, Z. Ali, I. ul Haq, A. Shah, J. Saudi Chem. Soc. 27 (2023) 101639.
[50] K. Mageshwari, R. Sathyamoorthy, Mater. Sci. Semicond. Process. 16 (2013) 337–343.
[51] Y. Altinay, A. Akkaya, R. Aydın, B. Şahin, Chemelectrochem 10 (2023) e202300208.
[52] P. Kumar, M. Chandra Mathpal, J. Prakash, B.C. Viljoen, W.D. Roos, H.C. Swart, J. Alloys Compd. 832 (2020) 154968.
[53] P. Brüesch, Phonons: Theory and Experiments I: Lattice Dynamics and Models of Interatomic Forces, Springer Berlin Heidelberg, Berlin, 1982.
[54] M.F.N. Taufique, A. Haque, P. Karnati, K. Ghosh, J. Electron. Mater. 47 (2018) 6731–6745.
[55] A.F. Abdulrahman, N.M. Abd-Alghafour, S.M. Ahmed, Sensor Actuator Phys. 323 (2021) 112656.
[56] M. Jay Chithra, M. Sathya, K. Pushpanathan, Acta Metall. Sin. 28 (2015) 394–404.
[57] L. Bergman, X.-B. Chen, J. Huso, J.L. Morrison, H. Hoeck, J. Appl. Phys. 98 (2005) 093507.
[58] R. Udayabhaskar, B. Karthikeyan, J. Appl. Phys. 115 (2014) 154303.
[59] T.C. Damen, S.P.S. Porto, B. Tell, Phys. Rev. 142 (1966) 570–574.
[60] F. Decremps, J. Pellicer-Porres, A.M. Saitta, J.-C. Chervin, A. Polian, Phys. Rev. B 65 (2002) 092101.
[61] A. Akkaya, B. Şahin, R. Aydın, H. Çetin, E. Ayyıldız, J. Mater. Sci. Mater. Electron. 31 (2020) 14400–14410.
[62] N.S. Kirik, B. Şahin, Micro and Nanostructures 167 (2022) 207290.
[63] R. Aydın, A. Akkaya, O. Kahveci, B. Şahin, ACS Omega 8 (2023) 20009–20019.
[64] H. Safdar, R. Aydın, B. Şahin, Ceram. Int. 48 (2022) 26678–26688.
[65] N. Widiarti, J.K. Sae, S. Wahyuni, IOP Conf. Ser. Mater. Sci. Eng. 172 (2017) 012036.
[66] E. Asfuroğlu Coşkun, B. Şahin, Sensor Actuator Phys. 328 (2021) 112770.
[67] P. Priyadarshini, S. Das, R. Naik, RSC Adv. 12 (2022) 9599–9620.
[68] M.E. Güldüren, D. İskenderoğlu, H. Güney, S. Morkoç Karadeniz, M. Acar, E. Gür, Int. J. Hydrogen Energy 48 (2023) 20804–20814.
[69] M.G. Althobaiti, S.S. Alharthi, A.N. Alharbi, A. Badawi, Appl. Phys. A 128 (2022) 539.
[70] R.H. Alshammari, M. Aadil, T. Kousar, U. Maqbool, Z. Ahmad, A.M. Alswieleh, T. S. Algarni, M. Naeem, Opt. Mater. 144 (2023) 114314.
[71] N. Narayanan, D. Nk, Mater. Res. 21 (2018) e20180034.
[72] M.K. Khalaf, B.A.M. Alhilli, A.I. Khudiar, A.A. Alzahra, Photon. Nanostruct: Fundam. Appl. 18 (2016) 59–66.
[73] S.M. Al-Shomar, Mater. Res. Express 7 (2020) 036409.
[74] M.-C. Jun, S.-U. Park, J.-H. Koh, Nanoscale Res. Lett. 7 (2012) 639.
[75] Wide Bandgap Semiconductors: Pursuing the Promise (DOE/EE-0910), 2013. U.S. D.o.E. (DOE.
[76] G.K. Reeves, H.B. Harrison, IEEE Electron. Device Lett. 3 (1982) 111–113.
[77] D.K. Schroder, Semiconductor Material and Device Characterization, John Wiley & Sons, New York, 2006.
[78] H. Murrmann, D. Widmann, IEEE Trans. Electron. Dev. 16 (1969) 1022–1024.
[79] J. Han, P.Q. Mantas, A.M.R. Senos, J. Eur. Ceram. Soc. 22 (2002) 49–59.
[80] A. López-Suárez, D. Acosta, C. Magaña, F. Hernández, J. Mater. Sci. Mater. Electron. 31 (2020) 7389–7397.
[81] E.R. Shaaban, M.Y. Hassaan, M.G. Moustafa, A. Qasem, E.S. Yousef, Appl. Phys. A 126 (2019) 34.
[82] M. Emam-Ismail, A.A. Gharieb, S.H. Moustafa, M.M. Mahasen, E.R. Shaaban, M. El-Hagary, J. Phys. Chem. Solid. 157 (2021) 110195.
[83] B. Şahin, R. Aydın, H. Çetin, Ceram. Int. 45 (2019) 16748–16758.